

Self-Gravity Driven Instabilities of Interfaces in the ISM

R.M. Hueckstaedt,^{1*} J.H. Hunter, Jr.,² and R.V.E. Lovelace³

¹ *Applied Physics Division, Los Alamos National Laboratory, Los Alamos, NM 87545, USA*

² *Department of Astronomy, University of Florida, Gainesville, FL 32611, USA*

³ *Departments of Applied Physics and Astronomy, Cornell University, Ithaca, NY 14853, USA*

29 October 2018

ABSTRACT

In order to understand star formation it is important to understand the dynamics of atomic and molecular clouds in the interstellar medium (ISM). Nonlinear hydrodynamic flows are a key component to the ISM. One route by which nonlinear flows arise is the onset and evolution of interfacial instabilities. Interfacial instabilities act to modify the interface between gas components at different densities and temperatures. Such an interface may be subject to a host of instabilities, including the Rayleigh-Taylor, Kelvin-Helmholtz, and Richtmyer-Meshkov instabilities. Recently, a new density interface instability was identified. This self-gravity interfacial instability (SGI) causes any displacement of the interface to grow on roughly a free-fall time scale, even when the perturbation wavelength is much less than the Jeans length. In previous work, we used numerical simulations to confirm the expectations of linear theory and examine the nonlinear evolution of the SGI. We now continue our study by generalizing our initial conditions to allow the acceleration due to self-gravity to be non-zero across the interface. We also consider the behaviour of the SGI for perturbation wavelengths near the Jeans wavelength. We conclude that the action of self-gravity across a density interface may play a significant role in the ISM either by fueling the growth of new instabilities or modifying the evolution of existing instabilities.

Key words: hydrodynamics — instabilities — turbulence — ISM:evolution — stars: formation

1 INTRODUCTION

Hydrodynamic instabilities of interfaces in the interstellar medium (ISM) have received renewed attention in part due to the remarkable Hubble images of “elephant trunks” and “pillars” in the Eagle Nebula (Hester et al. 1996; Pound 1998). Most of the theoretical and simulation work has focused on the stability/instability of ionization fronts driven by UV radiation of nearby OB stars (e.g., Mizuta et al. 2005; Williams 2002). The fronts may undergo acceleration so as to give the classical Rayleigh-Taylor instability but the influence of recombination may suppress the instability (Mizuta et al. 2005).

Hunter, Whitaker, and Lovelace (1997, 1998; hereafter Papers 1 and 2) studied the stability of interfaces in more quiescent regions of the ISM where the ionizing radiation is not important. They identified a new interfacial instability which is driven by self-gravity and acts at a density discontinuity. This self-gravity interfacial instability (SGI) persists in the static limit for all wavelengths and occurs in addition to the classical Rayleigh-Taylor instability. Us-

ing a normal mode analysis, they derived the linear growth rate of the SGI in compressible media in relative motion (allowing for the influence of Kelvin-Helmholtz instability). In the incompressible limit, the growth rate for a perturbation $\sim \exp(-i\omega t)$ of a planar interface is

$$\omega^2 = \frac{-2\pi G(\rho_2 - \rho_1)^2}{\rho_2 + \rho_1} + \frac{gk(\rho_2 - \rho_1)}{\rho_2 + \rho_1}. \quad (1)$$

In equation (1), k is the horizontal perturbation wave number ($k > 0$), g a constant background acceleration, and G the gravitational constant. The mass densities of the lower and upper fluids are specified as ρ_1 and ρ_2 , respectively. The second term gives the growth rate for the incompressible Rayleigh-Taylor (RT) instability, and the first term is the incompressible growth rate for the SGI. Both instabilities persist in the static limit, but several important differences are evident. Self-gravity knows no preferred direction, so the SGI is destabilizing across any density interface. An interface is RT unstable only if $g(\rho_2 - \rho_1) < 0$, such that the heavy fluid sits “on top” of the light fluid. The SGI growth rate depends upon the absolute densities of the fluids and their ratio but not the perturbation wavelength. The RT growth rate changes with perturbation wavelength and den-

* E-mail:rmhx@lanl.gov

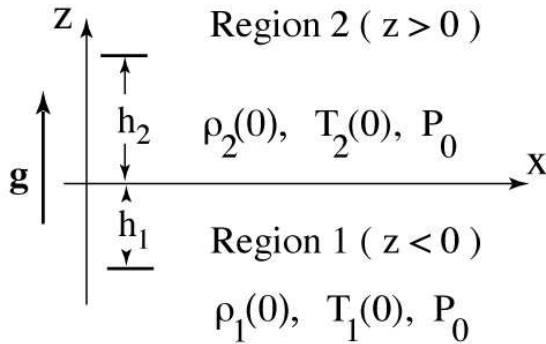


Figure 1. Schematic of the equilibrium configuration.

sity ratio, but it does not depend upon the absolute densities in the fluids. Given these dependencies, the SGI is expected to grow faster than the RT instability for a fixed value of g when the perturbation wavelength is long enough such that $\lambda = 2\pi/k > g/G|\rho_2 - \rho_1|$. In planar geometry, the growth rate for the SGI depends only weakly upon the Jeans criterion for the fully compressible case and not at all upon the perturbation wavelength in the incompressible limit. The underlying reason that self-gravity is able to drive an instability for any wave number is that the configuration is not one of minimum energy.

Numerical studies contrasting the behaviours of the SGI and RT instabilities have been performed by Hueckstaedt and Hunter (2001; Paper 3) and by Hueckstaedt, Peterson, and Hunter (2005; Paper 4). In the nonlinear regime, the SGI evolves such that the growth of tenuous bubbles outpaces that of dense spikes; whereas, the RT instability is characterized by dense spikes streaming into the tenuous fluid. In previous work, we sought to isolate the SGI by creating a set of hydrostatic initial conditions such that the pressure gradient and the acceleration due to self-gravity are both zero across the density interface. In the present work, we relax this restriction and allow them to be non-zero at the interface. The self-gravitational acceleration can effectively drive an RT-like instability provided the acceleration is in the same direction as the density gradient across the interface. Although the self-gravitational acceleration varies with position, it may be roughly constant near the interface where the growth is strongest. This RT-like instability cannot be strictly isolated because the SGI always will arise in the presence of a density interface. Notwithstanding, the growth rate of the RT-like instability can be adjusted to grow faster than the SGI by increasing the acceleration at the interface or decreasing the perturbation wavelength.

Section 2 describes the envisioned equilibrium configurations, while §3 describes the two-dimensional computer simulations. Section 4 discusses the results of our simulations, and §5 gives the conclusions of this work.

2 EQUILIBRIUM CONFIGURATION

In order to isolate the gravitational instabilities, simulations are begun from a state of hydrostatic equilibrium. The geometry of the problem is shown in Figure 1. The interfacial

values of the equilibrium densities and temperatures in the two regions are $\rho_1(0) > \rho_2(0)$ and $T_1(0) < T_2(0)$, and the interfacial pressure P_0 is the same for both media. The densities and pressures lapse to zero at heights h_1 below and h_2 above the interface. For RT simulations, a constant acceleration g is applied in the upward direction.

Adapting a polytropic equation of state ($P = \kappa\rho^\gamma$), exact equilibrium solutions for a self-gravitating gas exist in the one dimensional, unperturbed, planar problem when $\gamma = 2/3, 1, 2,$ and ∞ . A choice of $\gamma = 2$ results in a stiffer equation of state than is realistic for the ISM, but it admits simple, spatially bounded, analytic expressions for the equilibrium distributions. Previous studies revealed no differences in morphology or growth rate between simulations with $\gamma = 2$ and $\gamma = 1.4$ (Hueckstaedt 2001). For $\gamma = 2$, the hydrostatic and Poisson equations reduce to

$$\frac{d\rho_n(z)}{dz} = K_n f_n(z), \quad (2)$$

and

$$\frac{df_n(z)}{dz} = -4\pi G\rho_n(z). \quad (3)$$

In the above, $n = 1$ for region 1 and $n = 2$ for region 2, $K_n = [\rho_n(0)]^2/2P_0$, and $f_n(z)$ are the self-gravitational accelerations. The solutions for the densities and accelerations have the forms

$$\rho_n(z) = \rho_n(0) \cos\left(\frac{z}{l_n}\right) + \rho_n(0) \frac{f_0}{\beta} \sin\left(\frac{z}{l_n}\right), \quad (4)$$

and

$$f_n(z) = f_0 \cos\left(\frac{z}{l_n}\right) - \beta \sin\left(\frac{z}{l_n}\right). \quad (5)$$

The acceleration is continuous across the interface, $f_1(0) = f_2(0) = f_0$. The constant β is defined as

$$\beta = 2\sqrt{2\pi G P_0}. \quad (6)$$

The gravitational scale heights obey the relation

$$l_n = \frac{1}{\rho_n(0)} \sqrt{\frac{P_0}{2\pi G}}. \quad (7)$$

Defining h_1 and h_2 as the absolute values of the heights at which the density and pressure go to zero in the corresponding regions, the surface densities are

$$\sigma_2 \equiv \int_0^{h_2} \rho_2(z) dz = \frac{\beta}{4\pi G} \sin\left(\frac{h_2}{l_2}\right) + \frac{f_0}{4\pi G} \left[1 - \cos\left(\frac{h_2}{l_2}\right)\right], \quad (8)$$

and

$$\sigma_1 \equiv \int_{-h_1}^0 \rho_1(z) dz = \frac{\beta}{4\pi G} \sin\left(\frac{h_1}{l_1}\right) - \frac{f_0}{4\pi G} \left[1 - \cos\left(\frac{h_1}{l_1}\right)\right]. \quad (9)$$

Using equations (5), (8), and (9), it can be verified that Gauss' Theorem is satisfied,

$$f_2(h_2) - f_1(h_1) = -4\pi G(\sigma_2 + \sigma_1). \quad (10)$$

By symmetry, $f_2(h_2) = -f_1(h_1)$, which leads to the expression

$$f_2(h_2) = -2\pi G(\sigma_2 + \sigma_1). \quad (11)$$

Upon integrating equation (3) from $z = 0$ to $z = h_2$, we find

$$f_2(h_2) - f_0 = -4\pi G\sigma_2, \quad (12)$$

or

$$f_0 = 4\pi G\sigma_2 + f_2(h_2) = 4\pi G\sigma_2 - 2\pi G(\sigma_2 + \sigma_1), \quad (13)$$

or

$$f_0 = 2\pi G(\sigma_2 - \sigma_1). \quad (14)$$

Recalling that the densities in media 1 and 2 lapse to zero at $z = -h_1$ and $z = h_2$, respectively, it follows from equation (4) that

$$\tan\left(\frac{h_2}{l_2}\right) = -\frac{\beta}{f_0}, \quad (15)$$

and

$$\tan\left(\frac{h_1}{l_1}\right) = \frac{\beta}{f_0}. \quad (16)$$

Hereafter, we define $\theta_1 = h_1/l_1$ and $\theta_2 = h_2/l_2$, both greater than zero. The quadrants in which these angles are defined depends upon the sign of f_0 . If f_0 is greater than zero, θ_1 is in the first quadrant and θ_2 is in the second quadrant. Defining $\psi = \sqrt{\beta^2 + f_0^2}$, we have the relations $\sin \theta_1 = \beta/\psi$, $\cos \theta_1 = f_0/\psi$, $\theta_2 = \pi - \theta_1$, $\sin \theta_2 = \sin \theta_1$, and $\cos \theta_2 = -\cos \theta_1$. Therefore,

$$\sigma_2 = \frac{\beta^2 + f_0^2 + f_0\psi}{4\pi G\psi}, \quad (17)$$

and

$$\sigma_1 = \frac{\beta^2 + f_0^2 - f_0\psi}{4\pi G\psi}. \quad (18)$$

Consequently,

$$f_0 = 2\pi G(\sigma_2 - \sigma_1) = \frac{4\pi G f_0 \psi}{4\pi G \psi} = f_0, \quad (19)$$

an identity. The same process can be applied for the case $f_0 < 0$, with similar results. Therefore, the solutions form a consistent set.

In view of these results, we adopt the following strategy. We set the molecular weight to $\mu = 2$ for both media. We specify the densities and temperatures at the interface and calculate P_0 , β , l_1 , and l_2 . Then, we select f_0 and compute the density distributions from equation (4). The pressure and temperatures distributions follow from the equation of state. The final step is to use equation (5) to calculate the boundary values of $f_n(z)$ for use by the gravity solver.

Due to discretization of the distributions across the grid, a truly static state is not achieved. We deem the setup to be sufficiently static if the motions induced in the unperturbed case are negligible compared to any imposed velocity perturbations. For example, a typical set of initial values at the interface is: $\rho_1(0) = 10^{-20} \text{ g cm}^{-3}$, $T_1(0) = 20 \text{ K}$, $\rho_2(0) = 0.2 \times 10^{-20} \text{ g cm}^{-3}$, and $T_2(0) = 100 \text{ K}$. The adiabatic sound speed for a temperature of 20 K is $c = \sqrt{\gamma P_0/\rho_1(0)} = 40,800 \text{ cm s}^{-1}$. We typically use 5% of the sound speed (about 2040 cm s^{-1}) as the initial perturbation amplitude. If allowed to run to 5 e -folding times ($1.06 \times 10^{14} \text{ s}$), the highest velocities observed throughout the grid are less than 100 cm s^{-1} . (This represents a conservative case; most static models show lower velocities.) This is more than an order of magnitude lower than the initial velocity perturbation amplitude. Deviations from the static solutions are not large enough to affect the results of the perturbed simulations.

3 SIMULATIONS

As a test of the theory and for understanding the nonlinear behaviour of the instabilities we have carried out two-dimensional hydrodynamic simulations using CFDLib (Computational Fluid Dynamics Library), which was developed at the Los Alamos National Laboratory (Kashiwa et al. 1994). The system of equations we solve is

$$\begin{aligned} \frac{\partial \rho}{\partial t} + \nabla \cdot (\rho \mathbf{v}) &= 0, \\ \frac{\partial(\rho \mathbf{v})}{\partial t} + \nabla \cdot \mathcal{T} &= \rho \mathbf{g}, \end{aligned} \quad (20)$$

$$\frac{\partial}{\partial t} \left(\frac{1}{2} \rho \mathbf{v}^2 + \rho \varepsilon \right) + \nabla \cdot \left[\left(\frac{1}{2} \rho \mathbf{v}^2 + \rho w \right) \mathbf{v} \right] = 0,$$

$$\nabla \cdot \mathbf{g} = 4\pi G \rho,$$

where $\mathcal{T}_{jk} = p\delta_{jk} + \rho v_j v_k$ is the stress tensor, \mathbf{g} is the gravitational acceleration, ε is the specific energy of the fluid, $w = \varepsilon + p/\rho$ is the enthalpy, and the equation of state is $p = (\gamma - 1)\rho\varepsilon$. CFDLib is a finite-volume code well suited for problems of all flow speeds. The self-gravitational potential is solved for in two-dimensions using the MUDPACK multigrid code developed at the National Center for Atmospheric Research (Adams 1989, 1991). Models are run on a 2D Cartesian mesh of size 257×257 . Simulations repeated on a 513×513 grid show a difference in fine scale structure but not in growth rate. The normal velocity components of the gas are confined by reflective boundary conditions on all sides; whereas, the gravitational potential solver uses periodic boundary conditions along the side boundaries and specified gradient conditions along the top and bottom.

We induce perturbations along the interface through a velocity function of the form

$$v(x, z) = v_0 \cos(kx) \exp(-k|z|), \quad (21)$$

with v_0 set to 5% of the sound speed in the denser fluid. The perturbation is localized to the interface due to the exponential factor in the vertical, z -direction. We use a velocity perturbation instead of a spatial perturbation for two reasons. While our grid resolution is sufficient to determine growth rates and obtain a sensible picture of nonlinear structure, it is too coarse to impose a spatial perturbation without giving rise to spurious instabilities due to the square cell structure. Also, without careful consideration, imposing a perturbation across an interface gives rise to a decaying as well as a growing mode. The effect of the decaying mode upon the velocity is easily seen and considered in determining growth rates.

For ease of notation, we quote all times in units of the e -folding time for the incompressible, linear SGI ($g = 0$) as determined from equation (1), $t_e = \omega^{-1} = 2.11 \times 10^{13} \text{ s}$. We normalize all growth rates by dividing by the corresponding SGI growth rate, $\omega_{SGI} = t_e^{-1} = 4.73 \times 10^{-14} \text{ s}^{-1}$. We define two ratios for each model: Ω_S for the growth of dense spikes, and Ω_B for the growth of tenuous bubbles. We can define an average normalized growth rate $\Omega_T = 0.5(\Omega_B + \Omega_S)$. This language is consistent with typical RT descriptions.

For this study, we define two different classes of models. For the first suite of models, we selected a perturbation wavelength, $\lambda = 3.21 \times 10^{17} \text{ cm}$, a value nearly a

factor of ten smaller than the Jeans length in the denser fluid. We estimate the acceleration that would give rise to an RT instability with the same growth rate as the SGI, $g = \sqrt{2}G(\rho_1(0) - \rho_2(0))\lambda = 2.43 \times 10^{-10} \text{cm s}^{-2}$. (The factor $\sqrt{2}$ is a geometric correction to account for the use of a one-dimensional wave vector instead of a two-dimensional wave vector. The value of k is reduced by $\sqrt{2}$ in going from a 2D to a 1D wavevector, so the value of g must increase by $\sqrt{2}$ to arrive at the correct growth rate. By the same logic, we also adjust our definition of the Jeans wavelength in §4.3 to preserve the relationship $k\lambda = 2\pi$.) We compare the rate of perturbation growth for accelerated ($f_0 \neq 0$) interfaces against both the pure SGI ($f_0 = 0$) and RT ($g > 0$, no self-gravity) cases. Our strategy is to select f_0 values that should lead to growth rates equal to $q\omega_{SGI}$, where $q = 1, 2$, and 3. We compare the theoretical normalized growth rates q to the calculated values Ω_T . In addition, we look at models having $f_0 = -g \pm 1 \times 10^{-10} \text{cm s}^{-2}$, in order to ascertain the critical f_0 value defining the boundary between stable and unstable behaviour.

We follow with a second set of models designed to investigate the SGI as perturbation wavelengths approach the Jeans length. We remove the RT component ($f_0 = g = 0$) and use a value $\gamma = 1.1$ to allow more compression. When $f_0 = 0$, the initial distributions in density, temperature, and acceleration can be determined numerically for any value of γ (Hueckstaedt 2001). At question is whether the SGI can drive a system which is otherwise marginally Jeans stable toward global collapse.

4 RESULTS

In Papers 3 and 4, we compared and contrasted the growth of pure SGI and RT instabilities. An example of previous results is shown in Figure 2. Density contours for SGI and RT models with identical growth rates as determined by equation 1 are plotted for times of $2t_e$ and $4t_e$. As is characteristic of the SGI, the tenuous fingers grow more rapidly than the dense spikes. All of the models presented in this communication share the same theoretical e -folding time for a pure SGI instability, $t_e = \omega^{-1} = 2.11 \times 10^{13} \text{s}$. All times are quote in units of t_e . Figure 3 shows a typical velocity plot used to determine numerical growth rates. The logarithmic values of the maximum velocity in the spikes and bubbles are plotted for the RT instability. Lines are fit to the velocity points and slopes determined to represent the linear phase growth rates of both spikes and bubbles. Numerical growth rates for both the RT instability and SGI do not exactly match theoretical values. Rather, the ratio of computational to theoretical growth rate varies with velocity perturbation amplitude and density ratio across the interface (Paper 4).

4.1 Modifying growth rates with non-zero f_0

In order to generalize our study, we now allow non-zero values for f_0 . However, we do so without an imposed constant acceleration (i.e. no g term). So the RT-like contribution to the perturbation growth comes solely from the self-gravitational term at the interface. For $f_0 > 0$, an upward acceleration drives the interface in a RT-unstable manner. If $f_0 < 0$, the RT-like component is stabilizing, but since the

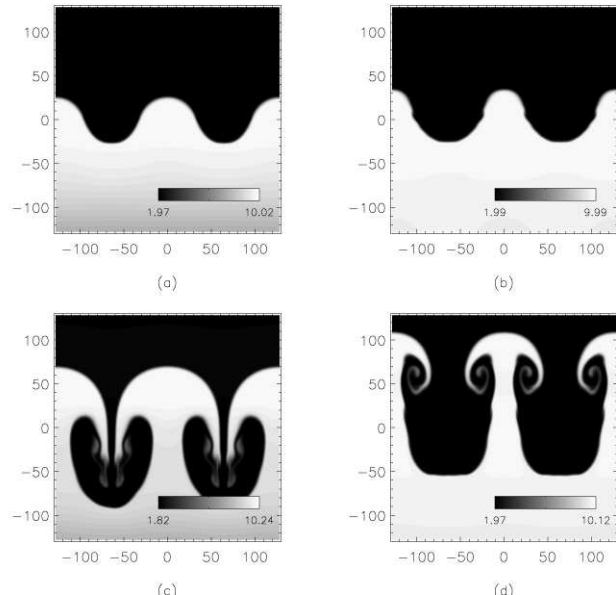


Figure 2. Density contours for the SGI [(a) and (c)] and the RT instability [(b) and (d)] for $t = 2t_e$ and $t = 4t_e$. The grey-scales show the density values $\times 10^{-21}$. The e -folding time $t_e = 2.11 \times 10^{13} \text{s}$ is determined from equation 1 and is used for all figures.

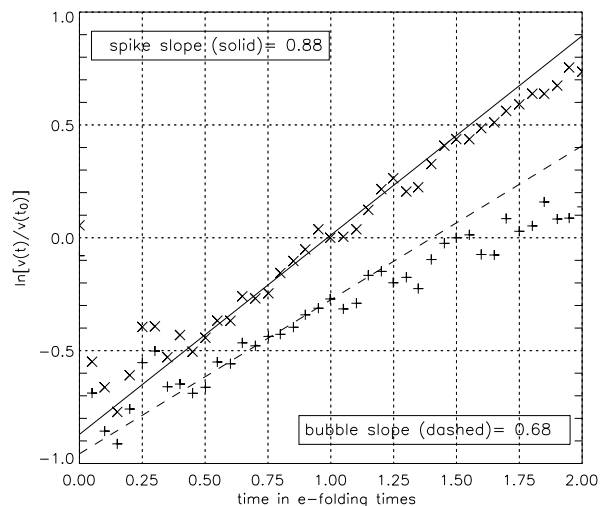


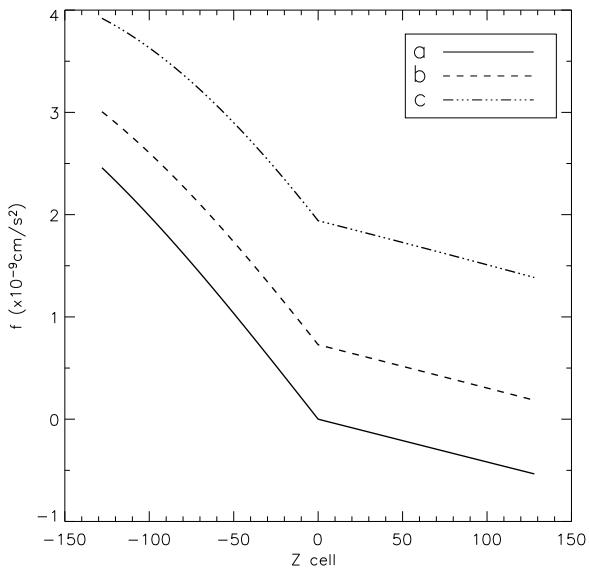
Figure 3. Velocity growth for RT instability. The maximum spike (\times) and bubble ($+$) velocities are plotted versus time using different values for the normalization velocity. Lines are drawn to represent the linear phase growth, with the slopes determining the growth rates.

SGI is always destabilizing, perturbations may still grow if the RT-like term is relatively small. We investigate the two issues with the set of models summarized in Table 1. First, we examine the overall growth rates when an unstable RT-like term is added to the SGI at the interface. Next we examine the marginal case where $f_0 = -g$ along with a small deviation in each direction.

The first study consists of three models: model f0 for

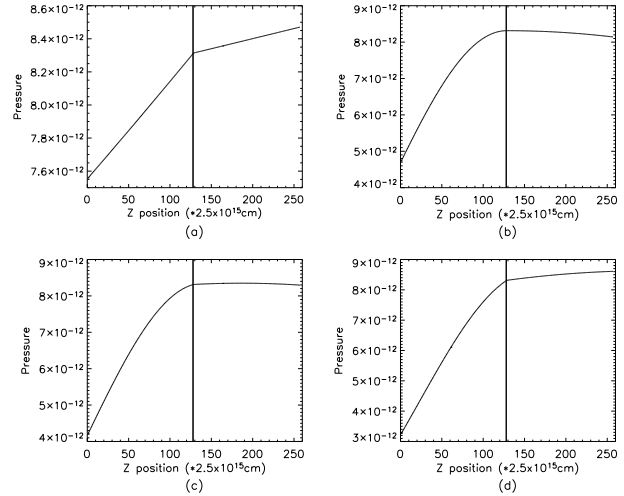
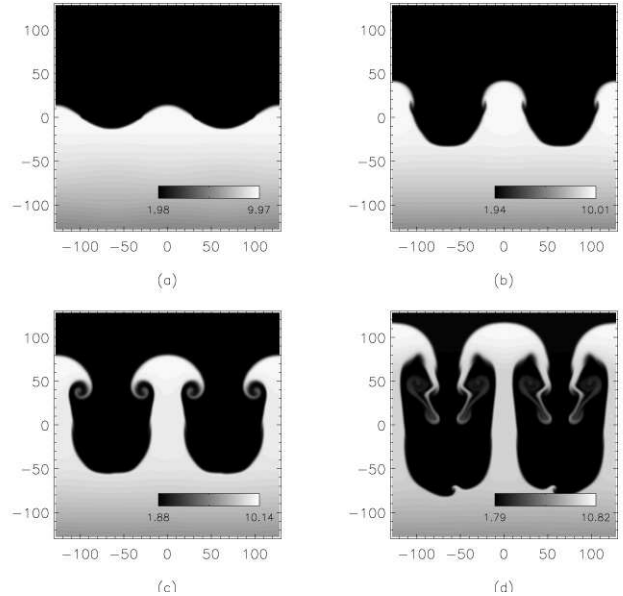
Table 1. Model Parameters

model	f_0	q	Ω_S	Ω_B	Ω_T	Figure #
f0	0.0	1	0.773	0.883	0.828	2
f3	7.277	2	1.800	1.529	1.665	6
f8	19.41	3	3.090	2.646	2.868	9
deq	-2.426	0	—	—	—	11
dpl	-1.426	—	—	—	—	—
dmi	-3.428	—	—	—	—	12

 Units for Table 1: $f_0 \rightarrow 10^{-10} \text{cm s}^{-2}$

Figure 4. Acceleration due to self-gravity (f) for (a) model f0: $f_0 = 0$, (b) model f3: $f_0 = 7.28 \times 10^{-10} \text{cm s}^{-2}$, and (c) model f8: $f_0 = 1.94 \times 10^{-9} \text{cm s}^{-2}$.

$f_0 = 0$, the pure SGI; model f3 for $f_0 = 7.28 \times 10^{-10} \text{cm s}^{-2}$, which is three times the value of g that would result in a pure RT instability with the same theoretical linear growth rate as model f0; and model f8 for $f_0 = 19.4 \times 10^{-10} \text{cm s}^{-2}$, with eight times the canonical value of g . The accelerations due to self-gravity at time zero for these three models are shown in Figure 4. A higher value of f_0 results in higher accelerations throughout the grid. The resultant equilibrium pressure distributions for these models (plus the pure RT instability) are shown in Figure 5. For the pure SGI, the pressure falls in both directions away from the interface. But as f_0 is increased, the acceleration in the less dense medium is positive instead of negative. As a result, a monotonically increasing pressure is required to form an equilibrium.

The values of f_0 for models f3 and f8 are chosen such that by equation (1) we expect twice and three times the growth rate, respectively, of model f0. In Figure 6 we show the evolution of model f3. Recall that the times are quoted in units of the e -folding time for model f0. A comparison of figures 6 and 2 shows that a non-zero value of f_0 does indeed lead to a hybrid sort of structure. The mushroom caps seen at later times are broader for model f3 than those in the pure RT case but slimmer than those in model f0. Also, the Kelvin-Helmholtz roll-ups in model f3 have assumed a


Figure 5. Initial pressure distributions for (a) RT instability with $g = 2.43 \times 10^{-10} \text{cm s}^{-2}$, (b) model f0, (c) model f3, and (d) model f8. The vertical lines indicate the interface locations.

Figure 6. Density contours for the SGI model f3 at (a) $0.9t_e$, (b) $1.5t_e$, (c) $2.1t_e$, and (d) $2.7t_e$.

more relaxed shape than the tight rolls seen in the pure RT. Velocity vectors are plotted for model f3 in Figures 7 and 8 at different times to illustrate the circulation patterns that develop.

The hybrid structure persists in model f8 (Figure 9). The mushroom caps are nearer in size than those in model f3 to the pure RT case, but the Kelvin-Helmholtz roll-ups retain their SGI-like relaxed shape. As listed in Table 1, both f3 and f8 have larger linear growth rates for the dense spikes than the bubbles ($\Omega_S > \Omega_B$). This is shown graphically for model f8 in Figure 10. In this respect, the RT-like growth induced by the relatively large values for f_0 dominate over the SGI component during the early phases of growth. For all three models, the calculated average growth rate Ω_T is a bit

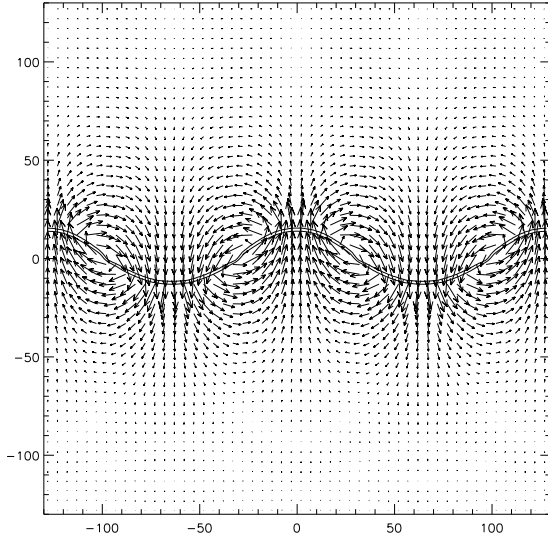


Figure 7. Velocity map for model f3 at $t = 0.9t_e$. Arbitrary density contours are overlotted to show the interface position.

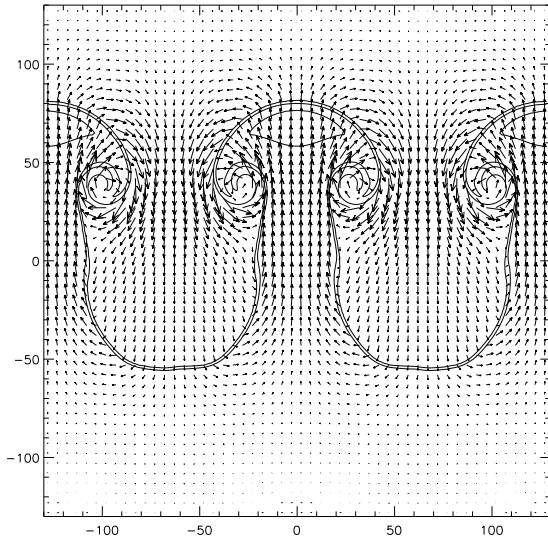


Figure 8. Velocity map for model f3 at $t = 2.1t_e$.

lower than the predicted q from simplified, incompressible theory. The calculated growth rate for model f3 is twice that for model f0, as expected. However, the calculated growth rate for model f8 is relatively high at nearly 3.5 times that of model f0. This larger than expected growth rate may be an indication that the amplified RT component grows too fast to be affected by the SGI component of the growth. We note that the calculated growth rate for spikes in model f8 ($\Omega_S = 3.09$) is three times the expected spike growth rate for a pure RT instability with $g = f_0$. Thus neither the SGI, nor deviations from incompressibility, appear to alter the rapid RT-like growth when f_0 is very large.

We now ask what happens if we apply a negative value of f_0 . In this case, $f_0(\rho_1 - \rho_2) < 0$ so the RT-like compo-

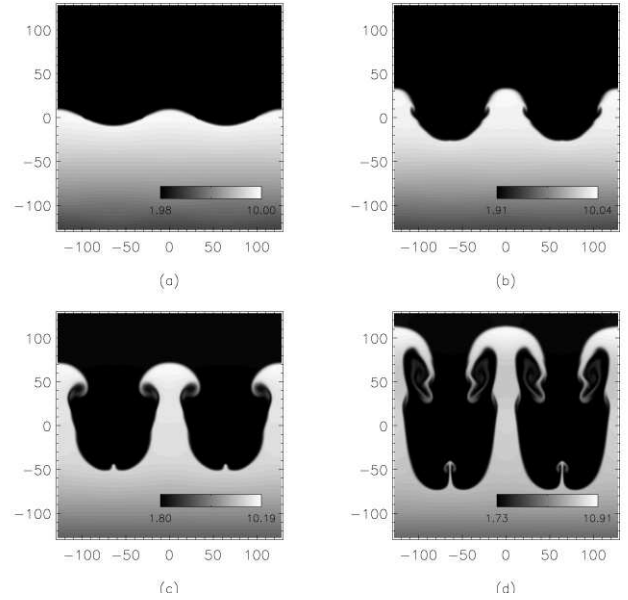


Figure 9. Density contours for the SGI model f8 at (a) $0.6t_e$, (b) $1.0t_e$, (c) $1.4t_e$, and (d) $1.8t_e$.

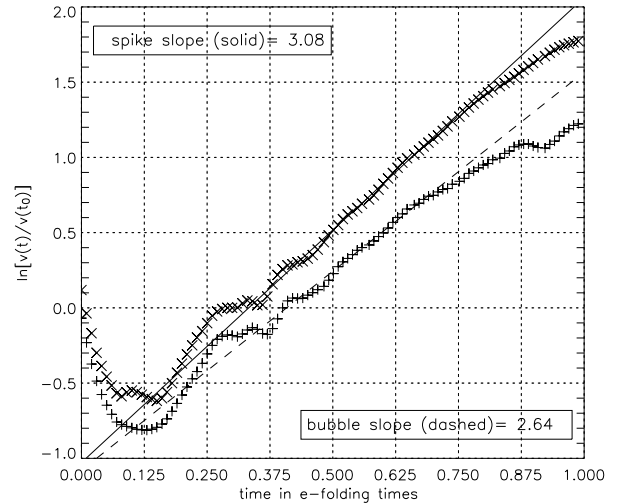


Figure 10. Velocity growth for model f8. The spike and bubble velocities are plotted with different normalization values.

nent is stabilizing. The evolution for model deq (Figure 11), for which $f_0 = -g$, is not quite stable even though incompressible theory predicts $q = 0$. The structure resembles the growth of the SGI more than that of the RT instability. The inherently unstable SGI seems more robust than the stabilizing RT component. If the RT component is weakened (decreased in absolute value), as in model dpl, the result is unchanged except for a slight increase in the rate of growth. If the RT component is increased in absolute value (model dmi), the SGI growth is quenched (Figure 12).

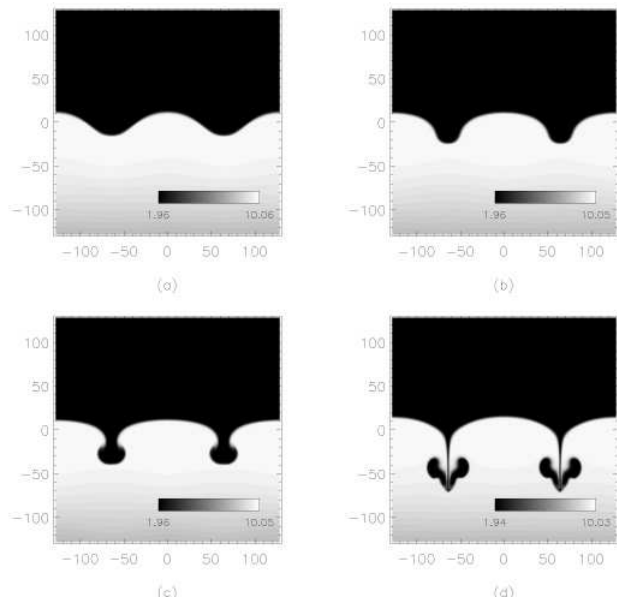


Figure 11. Density contours for the SGI with $f_0 = -g = -2.43 \times 10^{-10} \text{cm s}^{-2}$ at (a) $2.0t_e$, (b) $3.0t_e$, (c) $4.0t_e$, and (d) $5.0t_e$.

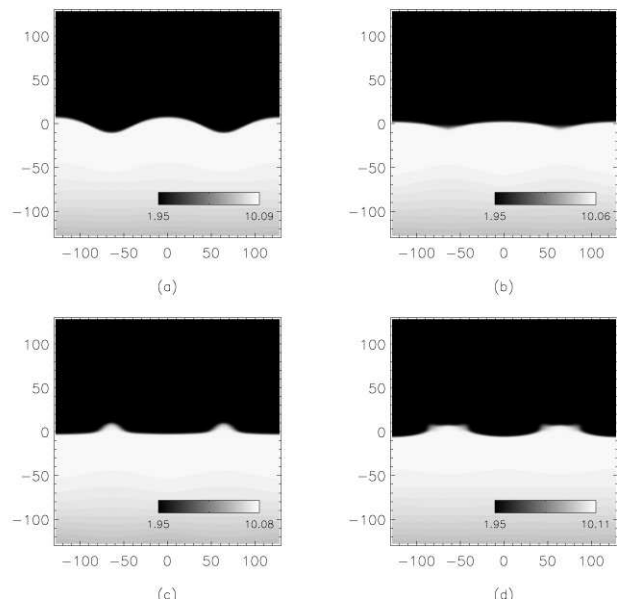


Figure 12. Density contours for the SGI with $f_0 = -3.43 \times 10^{-10} \text{cm s}^{-2}$ at (a) $2.0t_e$, (b) $3.0t_e$, (c) $4.0t_e$, and (d) $5.0t_e$.

4.2 Long wavelength perturbations with $\gamma = 1.1$

For another set of models, we decreased the ratio of specific heats and set $f_0 = 0$. We seek to examine the behaviour of the SGI as perturbation wavelengths approach the Jeans wavelength for gravitational collapse in the relatively dense, cool gas of medium 1 at the interface. We recall that the Jean wavelength (λ_J) is the wavelength at which the force of self-gravity exactly balances the stabilizing pressure force in an infinite, uniform, isothermal medium. Adjusting for non-unity γ , the three-dimensional Jeans length is given by $\lambda_{J3d} = \rho_1^{-1}(0) \sqrt{(\pi\gamma P_0)/G} = 2.07 \times 10^{18} \text{cm}$.

Table 2. Model Parameters

model	λ/λ_J	$\rho_{\max}(3t_e)$	$\rho_{\max}(6t_e)$	Figure #
LJ1	1	10.8	20.4	16
LJ2	1/2	10.7	12.2	13
LJ3	1/3	10.5	11.1	15

$\lambda_J = 2.92 \times 10^{18} \text{cm}$; densities given in units of $10^{-21} \text{g cm}^{-3}$

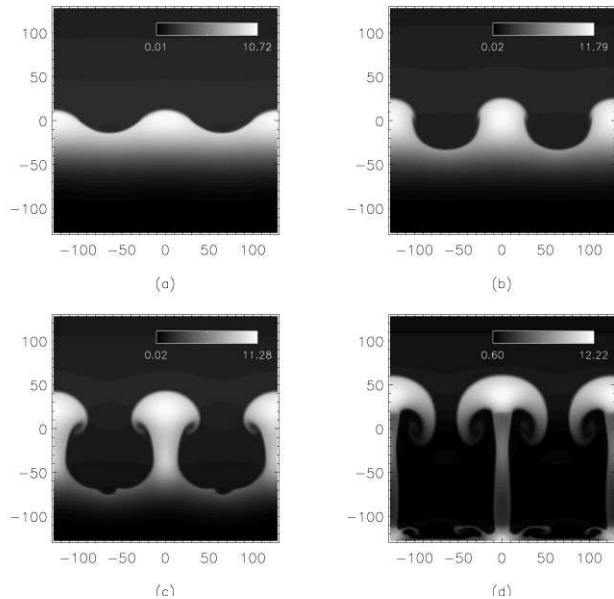


Figure 13. Density contours for the SGI model LJ2 with $\lambda = \lambda_J/2$ at (a) $3.0t_e$, (b) $4.0t_e$, (c) $5.0t_e$, and (d) $6.0t_e$.

We multiply this result by $\sqrt{2}$ to account for the two-dimensional nature of our simulations and arrive at the value $\lambda_J = 2.92 \times 10^{18} \text{cm}$. In an idealized model, no gravitational collapse is expected when $\lambda = \lambda_J$; a significantly longer wavelength is required for collapse to occur. In contrast, the SGI grows for all wavelengths, generating velocities which can lead to large compression if given an additional gravitational boost.

Other than the change to $\gamma = 1.1$, the physical parameters for the three models listed in Table 2 are identical to model f0. We increase the cell size in both directions to $\Delta x = \Delta y = 1.1373 \times 10^{16} \text{cm}$, so that the placement of two waves across 257 cells results in a perturbation wavelength $\lambda = \lambda_J/2$ (model LJ2). The evolution of this model is shown in Figure 13. The larger cell size results in poorer resolution of the roll-up features. This is the price paid to be able to examine large scale collapse behaviour without greatly increasing the computational cost. Velocity vectors for model LJ2 are shown in Figure 14 for $t = 5t_e$. By placing three waves across the 257 cell extent of the grid, we arrive at model LJ3 with $\lambda = \lambda_J/3$ (Figure 15). As expected, the shorter wavelength of model LJ3 results in a growth rate and morphology similar to those for model LJ2.

We observe different behaviour when $\lambda = \lambda_J$ (model LJ1). For this model, we extended the computational grid in the x direction to 513 cells and maintained the same cell size. As shown in Figure 16, the downward motion of the

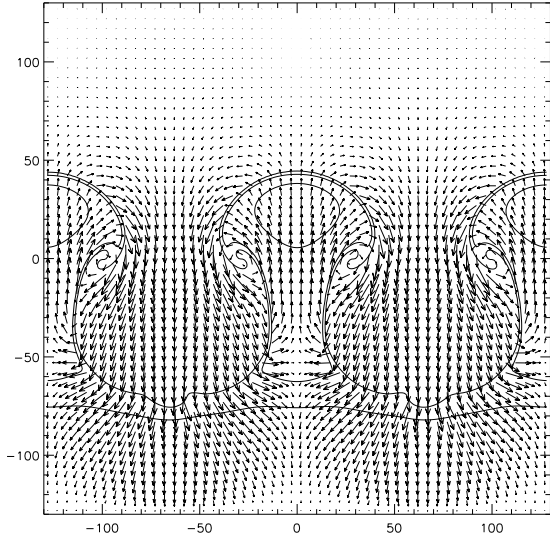


Figure 14. Velocity map for model LJ2 at $t = 5.0t_e$.

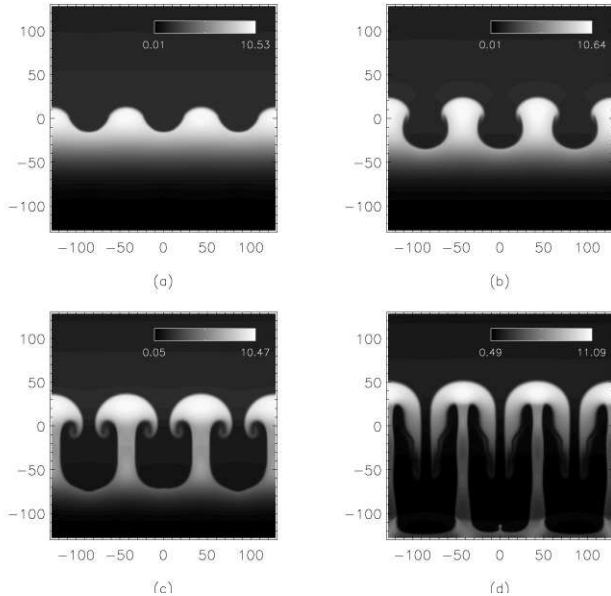


Figure 15. Density contours for the SGI model LJ3 with $\lambda = \lambda_J/3$ at (a) $3.0t_e$, (b) $4.0t_e$, (c) $5.0t_e$, and (d) $6.0t_e$.

tenuous bubbles (which outpaces the upward moving spikes in models LJ2 and LJ3) is slower than observed for the other models. Only the central part of the grid is shown in order to maintain a visual scale consistent with the previous figures. Velocity vectors for model LJ1 are shown in Figure 17 for $t = 5t_e$. Although the maximum velocities appearing in Figures 14 and 17 are comparable (about 0.4 km/s), model LJ1 exhibits a greater degree of collapse as indicated by the converging velocity vectors. The collapsing nature of model LJ1 is highlighted by taking density line-outs through dense columns for all three models at $t = 5t_e$ (Figure 18) and $t = 6t_e$ (Figure 19). The densest regions in models LJ2 and LJ3 are found in the dense mushroom caps which

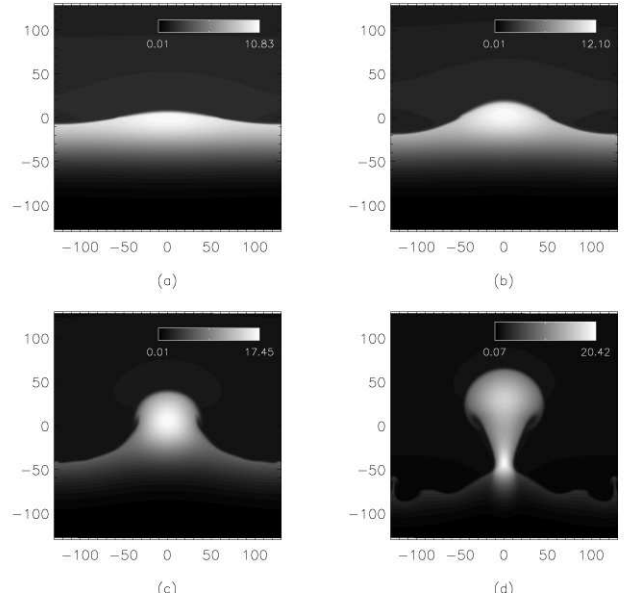


Figure 16. Density contours for the SGI model LJ1 with $\lambda = \lambda_J$ at (a) $3.0t_e$, (b) $4.0t_e$, (c) $5.0t_e$, and (d) $6.0t_e$.

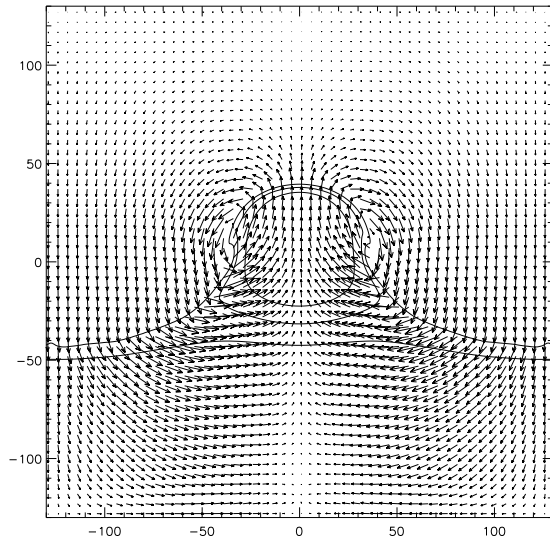


Figure 17. Velocity map for model LJ1 at $t = 5.0t_e$.

move upward over time. In model LJ1, the densest features form near the interface. At $t = 6t_e$, the highest compression is seen to have occurred at the stem of the spike rather than in the cap. We truncate our analysis at $t = 6t_e$ due to boundary effects from the top and bottom of the computational grid. Also, we consider the cylindrical symmetry of our two-dimensional calculations unrealistic after the onset of (three-dimensional) collapse. As an estimate of the minimum collapsing mass, we note that the mass of a sphere of diameter $\lambda_J/2$ (the positive phase of the perturbation for model LJ1) and uniform density $\rho_1(0)$ is about $8.2M_\odot$.

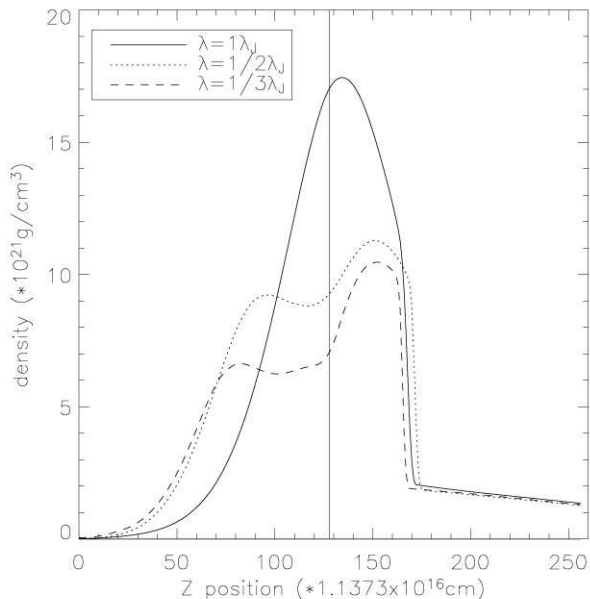


Figure 18. Density cuts through columns at $t = 5.0t_e$ for three different wavelengths. The vertical line indicates the initial location of the interface.

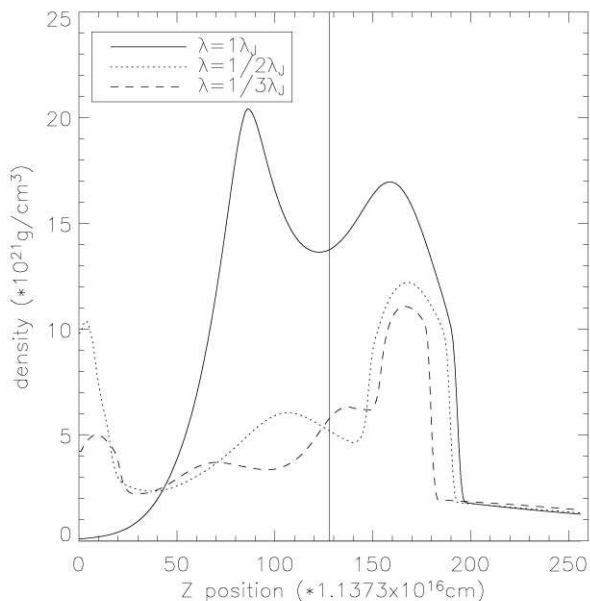


Figure 19. Density cuts through columns at $t = 6t_e$ for three different wavelengths.

5 CONCLUSIONS

Based upon the work summarized here, we conclude that large scale, planar density discontinuities (or near discontinuities) are inherently unstable on a gravitational collapse timescale in two respects: 1. Any density interface is inherently unstable to the SGI with a growth rate that is scale invariant for incompressible media and nearly scale invariant compressible media. (In compressible media, some of

the energy goes into compression at the expense of driving fluid displacement.) 2. In general, the acceleration due to self-gravity will be non-zero at a density interface, which will add a Rayleigh-Taylor component to the instability if $f_0(\rho_1 - \rho_2) > 0$. These instabilities cause crenulations along an interface to grow into spikes and bubbles with a growth rate and nonlinear structure that depend upon the relative strength of the SGI and RT-like components. For wavelengths that approach and exceed the Jeans length in the denser medium, structures initiated by interfacial instabilities are likely to undergo continued gravitational collapse.

An inspection of Hubble Telescope images of interstellar clouds reveals crenulated interfaces such as the “elephant trunks” and “pillars” in the Eagle Nebula (Hester et al. 1996; Pound 1998). These structures have commonly been interpreted in terms of the Rayleigh-Taylor instability of an ionization front created by the UV radiation from nearby OB stars, but without any consideration of the self-gravity of the cloud. However, recent simulations of the ionization front dynamics indicate that the Rayleigh-Taylor instability is quenched when hydrogen recombination is included (Mizuta et al. 2005) as predicted by Kahn (1958). It is clearly of interest to investigate the ionization front stability including self-gravity to see if the SGI instability overcomes the stabilizing effect of recombination. For this we would need to modify the third line of equation (20) to include the different energy sources and losses due to the UV absorption, recombination, and radiative cooling. It is also of interest to extend our work to larger computational grids which will allow us to follow perturbation growth to longer times. A more ambitious objective is to simulate the SGI in three-dimensions at both short and long wavelengths.

Gravitational processes (both global and interfacial) clearly have an important role in the evolving ISM. For example, Burkert and Hartmann (2004) have shown that gravitational forces give rise to a variety of structures along the edges of finite, self-gravitating sheets in a manner consistent with observations of local molecular clouds. In the final stages of star formation, gravitational forces dominate. But long before the final stages of collapse, gravitational forces are important for driving instabilities which convert gravitational energy into flow kinetic energy, enhance density inhomogeneities, and determine the partitioning of energy between different length scales.

ACKNOWLEDGMENTS

The authors thank B.A. Kashiwa and N.T. Padial for help in modifying CFDLib for astrophysical use. The work of R.L. was partially supported by CRDF grant KP2-2555-AL-03. Los Alamos National Laboratory is operated by the University of California for the U.S. Department of Energy under contract No. W-7405-Eng-36.

REFERENCES

- Adams, J. 1989, Applied Math. and Comput., 24, 113
- Adams, J. 1991, NCAR Technical Note 357+STR
- Burkert, A., & Hartmann, L. 2004, ApJ, 616, 288
- Hester, J.J., et al. 1996, AJ, 111, 2349

- Hueckstaedt, R.M., 2001, Ph.D. thesis, University of Florida
- Hueckstaedt, R.M., & Hunter, J.H., Jr. 2001, MNRAS, 327, 1097 (Paper 3)
- Hueckstaedt, R.M., Peterson, A.H., & Hunter, J.H., Jr. 2005, MNRAS, 361, L35 (Paper 4)
- Hunter, J.H., Jr., Whitaker, R.W., & Lovelace, R.V.E., 1997, ApJ, 482, 852 (Paper 1)
- Hunter, J.H., Jr., Whitaker, R.W., & Lovelace, R.V.E. 1998, ApJ, 508, 680 (Paper 2)
- Kahn, F.D. 1958, Rev. Mod. Phys., 30, 1058
- Kashiwa, B.A., Padial, N.T., Rauenzahn, R.M., & Vanderheyden, W.B. 1994, in ASME Symposium on Numerical Methods for Multiphas Flow, ed. C.T. Crowe (New York, ASME)
- Mizuta, A., Kane, J.O., Pound, M.W., Remington, B.A., Ryutov, D.D., & Takabe, H. 2005, 621, 803
- Pound, M.W. 1998, ApJ, 493, L113
- Williams, R.J.R. 2002, MNRAS, 331, 693